Interaction-Free Measurement with Electrons

Amy E. Turner[,1,*] Cameron W. Johnson[,1] Pieter Kruit[,2] and Benjamin J. McMorran[1]

[1]*Department of Physics, University of Oregon, Eugene, Oregon 97403, USA*
[2]*Department of Imaging Physics, Delft University of Technology, Lorentzweg 1, 2628CJ Delft, Netherlands*

Here, we experimentally demonstrate interaction-free measurements with electrons using a novel electron Mach-Zehnder interferometer. The flexible two-grating electron interferometer is constructed in a conventional transmission electron microscope and achieves high contrast in discrete output detectors, tunable alignment with independently movable beam splitters, and scanning capabilities for imaging. With this path-separated electron interferometer, which closely matches theoretical expectations, we demonstrate electron interaction-free measurements with an efficiency of $14 \pm 1\%$. Implementing this quantum protocol in electron imaging opens a path toward interaction-free electron microscopy.

Introduction.—The quantum bomb tester proposed by Elitzur and Vaidman was named one of the seven wonders of the quantum world, because it exploits the nonlocality and self-interference of a particle to noninteractively detect an object [1,2]. In this thought experiment, Elitzur and Vaidman considered the use of an interferometer to detect the presence of a bomb so sensitive that even a single probing particle could trigger it. The interferometer is configured such that the wave function of a probing particle traverses a superposition of two paths that destructively interfere at one of the outputs, the dark port, and constructively interfere at the other, the bright port [Fig. 1(a)]. The interference is disrupted if an opaque object obstructs one of the interferometer paths, increasing the probability of a detection event at the dark port—the outcome corresponding to an interaction-free measurement (IFM) of the object [Fig. 1(b)]. Here, we use a flexible, path-separated electron interferometer with good contrast between discrete output detectors to demonstrate the first experimental IFM with electrons.

IFMs have been demonstrated experimentally with photons [3], neutrons [4], and neutral atoms [5] but never before with charged particles such as electrons, which interact uniquely with matter and electromagnetic potentials. Electrons can be focused to much finer length scales, enabling widely used nanoscale and atomic resolution electron microscopies. Electron IFM configurations have recently been proposed for high-resolution, damage-free electron microscopy [6,7], which would improve imaging of radiation-sensitive samples such as biomolecules [8]. Interaction-free imaging with photons [9] has been shown to reduce the dose required to image semitransparent phase and amplitude samples [10–15], even in lossy experiments [16,17]; these protocols could revolutionize electron microscopy. Proposals to reduce the electron dose to theoretical limits feature advanced reillumination and

multipass designs [18,19] that require substantial advancements in electron optics. To progress toward fully interaction-free designs, we developed a suitable electron matter wave interferometer to complete a single-pass proof-of-principle experiment.

Electron interferometers constructed using electrostatic biprisms as wavefront-dividing beam splitters have provided high-resolution phase images for decades [20–22] in a technique called electron holography. Multiple biprisms have been employed to provide separated path geometries [23,24]. However, these biprism beam splitters are not conducive to efficient IFMs, because they do not provide discrete interferometer outputs—in electron holography, the interference pattern is imaged directly. In principle, an IFM could be demonstrated in such a setup by defining the dark detector to be the narrow strips along each dark trough of the sinusoidal interferogram, yet there would be an inherent trade-off between detection efficiency of IFM events and errant detections. Efficient, real-time IFMs require an interferometer with discrete outputs.

The earliest Mach-Zehnder electron interferometer with discrete outputs was constructed of single crystals [25].
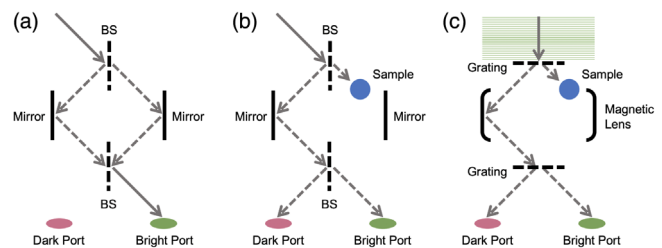

FIG. 1. Schematic of an optical Mach-Zehnder interferometer (a),(b) juxtaposed with the electron two-grating interferometer (c). The first two schematics (a),(b) illustrate the effect of an opaque sample on the output of a Mach-Zehnder interferometer.

Decades later, two crystals were imaged onto each other in a transmission electron microscope (TEM) to create an interferometer [26,27], with more recent implementations built from a monolithic crystal [28,29], but these compact interferometers are not adjustable and are difficult to use for imaging applications. Independently adjustable nanoscale gratings were used in a custom low-energy electron Mach-Zehnder interferometer [30]. Electron interferometers using a single phase grating as a beam splitter in a TEM achieved high-resolution imaging by directly recording interference patterns [31,32]. These experiments were made possible due to improvements in nanofabricating diffraction grating holograms, which are now more efficient and are precisely milled to shape the electron beam [33,34].

In this Letter, we construct and discuss a novel two-grating electron Mach-Zehnder interferometer in a conventional field emission TEM with discrete, complementary outputs like traditional optical Mach-Zehnder interferometers (Fig. 1). We adjust the relative phase in our interferometer and compare the output to both theory and simulation. This electron interferometer has high contrast in discrete output detectors, independently movable beam splitters, and scanning capabilities for imaging, which opens doors for future electron interferometric research and quantum measurement protocols. Here, we employ the flexible, path-separated electron interferometer to demonstrate the first experimental IFM with electrons.

Flexible two-grating interferometer.—Modern TEMs provide a versatile, highly configurable platform for

coherent electron optics experiments [35]. Whereas an optical Mach-Zehnder interferometer uses partially reflecting mirrors as beam splitters and fully reflecting mirrors to redirect the separate paths, here we use nanofabricated phase gratings as electron beam splitters and magnetic lenses to redirect the electron paths, as shown in Fig. 2(a). Both nanogratings consist of shaped grooves milled to precise depths into freestanding, thin silicon nitride membranes [Figs. 2(c) and 2(e)] [34]. Each grating is installed in an available TEM aperture which allows the gratings to be independently manipulated in the transverse plane.

Incident electron wave functions transmitted through the input grating coherently divide into multiple diffraction orders. The input grating has a blazed profile that forms two primary interferometer paths, the −1st and 0th diffraction orders, of nearly equal current [Figs. 2(c) and 2(d)]. Positive diffraction orders with smaller amplitudes are also present but are blocked with an aperture. Analyzing the interaction (0th), reference (−1st), and negative higher-ordered probes, the input current to the interferometer splits such that $52 \pm 3\%$, $46 \pm 3\%$, and $2 \pm 1\%$ is diverted into each path, respectively. Thus, if an object were present, the probability of an interaction is $P_{\text{int}} = 0.52 \pm 0.03$. A magnetic lens after the input grating focuses these diffraction orders down to sharply peaked probes at the interaction plane. The probe spacing for this configuration is on the order of hundreds of nanometers.

A second magnetic lens system defocuses and overlaps the multiple paths, projecting the resulting interference
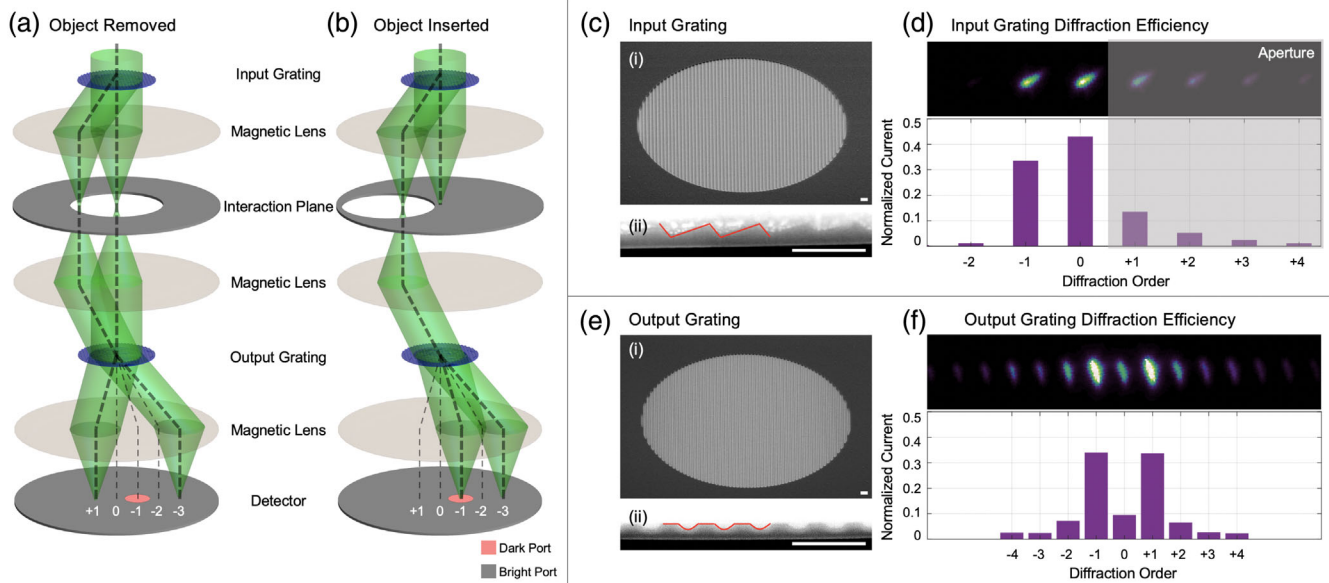

FIG. 2. Schematic of an electron two-grating interferometer in a TEM (not to scale) with the object removed (a) and inserted (b), overlayed with ray diagrams. The detector coloring illustrates the selectable regions on the camera that define the bright and dark output ports. The interferometer relies on nanofabricated diffraction gratings as beam splitters, both blazed (c),(d) and binary (e),(f). The full gratings (i) and capped cross sections (ii) are shown; the red lines highlight the profiles muddled by the platinum cap. All scale bars represent 400 nm. (d),(f) Raw images of the diffracted outputs of the two gratings used in the interferometer and their diffraction efficiencies below. The two-path interferometer is constructed by inserting an aperture, as shown in (d).

pattern onto the output grating. In this case, we chose to use a symmetric binary phase grating for the output beam splitter designed to yield two primary diffraction orders (-1 and $+1$) with the same angular separation as those from the input grating [Figs. 2(e) and 2(f)]. To reach the necessary alignment conditions, the image of the input grating formed by the interference of all diffraction orders is projected onto the output grating such that $2p_1 = p_2$, where p_1 and p_2 are the pitches of the input and output gratings, respectively. The interferometer output is directly imaged using the final lenses to project the far-field diffraction pattern onto a scintillator screen optically coupled to a CCD at the bottom of the TEM column. For a more detailed description of the microscope configuration, see Methods.

The far-field diffraction pattern from the aligned two-grating configuration results in isolated beams that constructively and destructively interfere at the detector. As the output grating is laterally shifted by a distance δx_2, the probability P_n of an event in each diffraction order n is periodic over the interval, $\delta x_2/p_1 \in [0, 1]$:

$$P_n(\delta x_2) \propto \frac{TI_n}{2}\left[1 + V_n \cos\left(\frac{2\pi\delta x_2}{p_1} + \phi_n\right)\right], \quad (1)$$

where T is the coherent transmission coefficient of the output grating and I_n, $V_n \in (0, 1]$, and ϕ_n are the current, visibility, and phase, respectively. The nth output diffraction order is determined by the Fourier coefficients of the two phase gratings chosen during nanofabrication [33,34] and then measured experimentally [Figs. 2(d) and 2(f)]. We find that the second grating coherently transmits $T = 60 \pm 3\%$ of incident electrons. This is the main source of inefficiency in our IFM experiment, but it can be improved with refined gratings [34] or lossless diffraction elements [36,37].

A dark port and bright port, similar to an optical Mach-Zehnder interferometer, can now be established. Because the blazed grating has an asymmetric output and the binary grating has a symmetric output, it is the -1 diffraction order that has highest contrast and complete destructive interference. Thus, the pixels of the detector that enclose the -1 diffraction order up to halfway to the adjacent diffraction orders are defined as the dark port (DP) detector such that $P_{\mathrm{DP}} = P_{-1}$. All other pixels on the detector are labeled as the bright port (BP) such that $P_{\mathrm{BP}} = \sum_{n\neq-1} P_n$ (as denoted by the colored regions on the left in Fig. 3). The position $\delta x_2/p_1$ of the output grating is tuned such that the -1 diffraction order at the detector is minimized, denoted by the vertical dashed lines in Fig. 3.

Interaction-free measurement.—To demonstrate IFMs, we use the edge of a platinum aperture as the opaque target object that selectively blocks one of the two interferometer paths, as shown in Fig. 2(b). When the object (knife edge) is inserted, the rate of total events at the output decreases. Yet, the number of events at the dark port *increases* due to
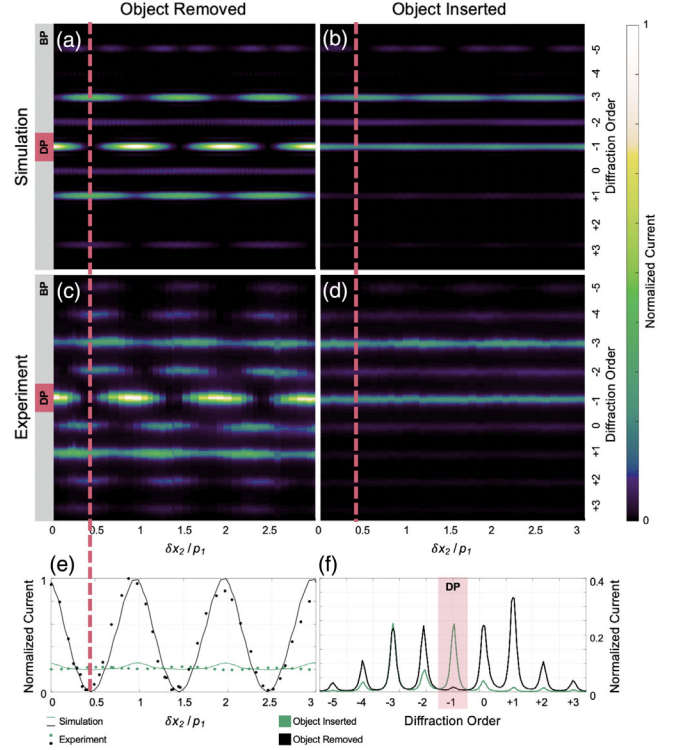

FIG. 3. Simulated (a),(b) and experimental (c),(d) output diffraction profiles of a two-grating interferometer as the second grating is moved relative to the projection of the top grating. The relative grating shift is reported as a fraction of the blazed grating pitch, $\delta x_2/p_1$. The left column (a),(c) shows the output currents for the object removed—the two-path case. The right column (b),(d) shows the output currents for the object inserted—the one-path case. The colored regions on the left illustrate the defined dark port (pink) and bright port (gray) regions of the detector. The dashed pink line illustrates an interaction-free measurement alignment. All values are normalized to the maximum pixel current in the two-path case. (e) The normalized dark port current as a function of the relative grating shift. (f) The experimental diffraction profile along the dashed pink line with the dark port highlighted.

there no longer being destructive interference at the output—the hallmark sign of quantum IFMs. Ideally, the output diffraction pattern would be unvarying when shifting the output grating with an object inserted. However, the position of the second grating subtly modifies the output diffraction pattern due to the interference between the faint higher orders and the dominant reference path, shown in Figs. 3(b) and 3(d). Regardless, the dark port events increase significantly.

Here, we compare the dark and bright port events with the object inserted and removed. All values are normalized to the total detector intensity for the two-path case and a one-second exposure. All error bars are the standard deviation from multiple measurements at different IFM alignments. As seen in Fig. 4, when the object is removed, the dark port holds $1.2 \pm 0.1\%$ of the events detected during an exposure. When an object is inserted to block one
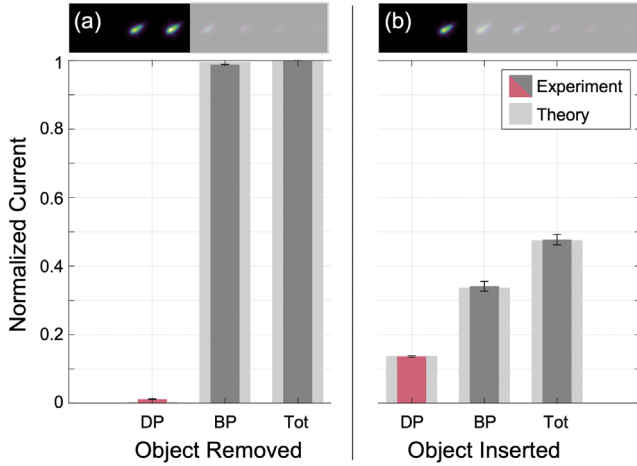
FIG. 4. Normalized output currents of a properly aligned two-grating interferometer with the object (a) removed and (b) inserted. The top row contains raw images of the interaction plane with a mock aperture to illustrate the object's position. The bar chart displays the DP, BP, and total (Tot) current in each configuration, normalized to the maximum output of the two-path configuration [Tot in (a)]. The light gray bars show the expected outputs from simulation. The error bars are the standard deviation of multiple measurements in distinct alignments.

interferometer path, the dark port event rate increases to $13.6 \pm 0.2\%$ relative to the two-path total event rate.

For each electron entering our interferometer when an object is present, the outcome probability of a dark port event (an IFM) is $P_{DP} = 0.082 \pm 0.004$, an interaction event $P_{int} = 0.52 \pm 0.03$, a bright port event $P_{BP} = 0.20 \pm 0.01$, and an electron scattered out of the experiment by the second grating $P_{loss} = 0.19 \pm 0.02$. The probability P_{NI} of no interaction and a dark port detection count using multiple electrons or sample reillumination [4] is $P_{NI} = P_{DP} \sum_{n=0}^{\infty} [P_{BP}]^n = 10.3 \pm 0.5\%$. In this initial demonstration, the incoherent scattering significantly reduces the IFM signal, though this could be minimized with improved beam splitters or eliminated with lossless diffractive elements [36,38].

The probabilities reported above disregard the inefficiency of the electron detector, which also results in IFM signal loss. The detective quantum efficiency (DQE) of our imaging detector at this beam energy can be greater than 0.5 [39–42], but collecting multiple events over longer exposure times provides better statistics. Future experiments will use improved detectors with single-electron sensitivity and a DQE approaching unity [43–45]. For a given detector, our experiment demonstrates that the fraction of *detected* events that can be interaction-free [3] is $\eta = P_{DP}/(P_{DP} + P_{int}) = 14 \pm 1\%$. Because of the incomplete suppression of the dark port during alignment, there is a small probability error that a dark port detection will misidentify the sample $P_E = P_{DP}^{SR}/P_{DP}^{SI} = 8.8 \pm 0.7\%$, where SI and SR denote sample inserted and sample removed, respectively.

Even with single-particle sensitivity and optimized beam splitters, an interaction event is more likely than a dark port event in a single-pass IFM experiment; thus, there is ongoing conversation about what constitutes an "interaction-free" measurement [46]. We do not utilize a single-electron source, but we emphasize that, with a beam current on the order of 50 pA and a longitudinal coherence length on the order of microns, there was about one electron in the microscope at a time. Recording single-electron IFM events has diminished value given a thermal source, though it can still enable reduced-dose imaging [19]. Our detector is not capable of single-electron detection, but the reported signal is directly proportional to the rate of single electrons arriving at the detector, analogous to previous IFM demonstrations using light [9]. The dark port signal is a record of electrons that did not interact with the object yet indicate its presence and, thus, reasonably demonstrates interaction-free measurements.

Conclusion.—In this Letter, we report the first quantum bomb tester with electrons. This was enabled by the inclusion of two independently movable nanofabricated phase gratings in a conventional TEM to create an electron Mach-Zehnder interferometer. This versatile electron interferometer is path separated at the sample and detector, with high contrast in the discrete outputs. Furthermore, the interferometer can be configured to incorporate scanning, which enables interferometric imaging. The demonstrated IFM efficiency $\eta = 14 \pm 1\%$ (with an overall IFM detection probability of $P_{DP} = 8.2\%$) is less than the optimal efficiency ($\eta_o = 33\%$) of a single-pass Mach-Zehnder interferometer using 50/50 beam splitters. However, it is a significant signal even with an error probability of $P_E = 8.8 \pm 0.7\%$. The undesired higher diffraction orders produced by the holograms, unequal splitting into the two interferometer paths, and incoherent scattering at the second beam splitter grating decrease the efficiency of our system. Fortunately, the behavior of the interferometer is well modeled using standard Fourier analysis in linear optics, which provides a path to hone grating nanofabrication, increase the interferometer efficiency, and decrease the number of errant detections.

The flexible two-grating interferometer can be utilized for inelastic interferometry, direct phase imaging [32], magnetic imaging [47,48], Aharonov-Bohm experiments [49,50], and low-dose imaging [19,51]. Furthermore, the electron interferometer enables interaction-free microscopy at the subnanometer length scale. The interferometers dose limits for imaging beam-sensitive materials could be characterized [52] by looking at the fading electron diffraction spots of a degrading material [53–55] or by observing chemical changes using electron energy-loss spectroscopy [56] in materials such as poly(methyl methacrylate). More advanced multipass electron IFM implementations will reduce the interactions to zero [6,7,18]. By applying quantum protocols to TEM imaging, the tension

between high-resolution and damage-free imaging is reduced, which opens a path toward imaging individual biological structures at atomic resolution with negligible damage [6,7].

Methods.—This experiment was conducted in an FEI Titan 80–300 TEM with a field emission source, operated at 80 keV. An FEI Helios dual-beam FIB was used to mill the input and output diffraction grating holograms into 50-nm-thick silicon nitride membranes coated with a thin charge alleviation layer. The input blazed grating had a diameter of 50 μm and a pitch of 200 nm. The input grating was inserted into the second condenser aperture. The TEM condenser lens settings were adjusted to form probes at the third condenser aperture, which was used as the beam-blocking interaction object in this Letter. The binary output grating had a diameter of 20 μm and a pitch of 800 nm. The output grating was held by a single tilt sample holder and inserted like a traditional TEM sample; thus, the second grating could be transversely shifted similar to a sample. The objective lens was turned off such that the objective aperture could be used to limit the field of view. A 20 μm objective aperture was inserted to select for the most coherent and well-aligned portion of the overlapping gratings. The projection and diffraction lenses were used to project the output diffraction pattern of the overlapped gratings onto the camera, a CCD at the bottom of the TEM column. The dark and bright port detectors were isolated regions of pixels on the camera defined during postprocessing.

———

*aturner2@uoregon.edu

[1] A. C. Elitzur and L. Vaidman, Quantum mechanical interaction-free measurements, Found. Phys. **23**, 987 (1993).

[2] M. Brooks, Weirdest of the weird, New Sci. **206**, 36 (2010).

[3] P. Kwiat, H. Weinfurter, T. Herzog, A. Zeilinger, and M. A. Kasevich, Interaction-Free Measurement, Phys. Rev. Lett. **74**, 4763 (1995).

[4] M. Hafner and J. Summhammer, Experiment on interaction-free measurement in neutron interferometry, Phys. Lett. A **235**, 563 (1997).

[5] C. Robens, W. Alt, C. Emary, D. Meschede, and A. Alberti, Atomic "bomb testing": the Elitzur—Vaidman experiment violates the Leggett—Garg inequality, Appl. Phys. B **123**, 12 (2017).

[6] P. Kruit, R. Hobbs, C.-S. Kim, Y. Yang, V. Manfrinato, J. Hammer, S. Thomas, P. Weber, B. Klopfer, C. Kohstall, T. Juffmann, M. Kasevich, P. Hommelhoff, and K. Berggren,

Designs for a quantum electron microscope, Ultramicroscopy **164**, 31 (2016).

[7] W. P. Putnam and M. F. Yanik, Noninvasive electron microscopy with interaction-free quantum measurements, Phys. Rev. A **80**, 040902(R) (2009).

[8] L. A. Baker and J. L. Rubinstein, Radiation damage in electron cryomicroscopy, in *Methods in Enzymology* (Elsevier, New York, 2010), Vol. 481, pp. 371–388, https://doi.org/10.1016/S0076-6879(10)81015-8.

[9] A. G. White, J. R. Mitchell, O. Nairz, and P. G. Kwiat, "Interaction-free" imaging, Phys. Rev. A **58**, 605 (1998).

[10] G. Krenn, J. Summhammer, and K. Svozil, Interferometric information gain versus interaction-free measurement, Phys. Rev. A **61**, 052102 (2000).

[11] S. Massar, G. Mitchison, and S. Pironio, Minimal absorption measurements, Phys. Rev. A **64**, 062303 (2001).

[12] G. Mitchison and S. Massar, Absorption-free discrimination between semitransparent objects, Phys. Rev. A **63**, 032105 (2001).

[13] G. Mitchison, S. Massar, and S. Pironio, Minimum number of photons needed to distinguish two transparencies, Phys. Rev. A **65**, 022110 (2002).

[14] P. Facchi, Z. Hradil, G. Krenn, S. Pascazio, and J. Řeháček, Quantum zeno tomography, Phys. Rev. A **66**, 012110 (2002).

[15] S. Thomas, C. Kohstall, P. Kruit, and P. Hommelhoff, Semitransparency in interaction-free measurements, Phys. Rev. A **90**, 053840 (2014).

[16] J.-S. Jang, Optical interaction-free measurement of semitransparent objects, Phys. Rev. A **59**, 2322 (1999).

[17] T. Rudolph, Better Schemes for Quantum Interrogation in Lossy Experiments, Phys. Rev. Lett. **85**, 2925 (2000).

[18] T. Juffmann, S. A. Koppell, B. B. Klopfer, C. Ophus, R. M. Glaeser, and M. A. Kasevich, Multi-pass transmission electron microscopy, Sci. Rep. **7**, 1699 (2017).

[19] A. Agarwal, K. K. Berggren, Y. J. van Staaden, and V. K. Goyal, Reduced damage in electron microscopy by using interaction-free measurement and conditional reillumination, Phys. Rev. A **99**, 063809 (2019).

[20] E. Völkl and H. Lichte, Electron holograms for subångström point resolution, Ultramicroscopy **32**, 177 (1990).

[21] A. Orchowski, W. D. Rau, and H. Lichte, Electron Holography Surmounts Resolution Limit of Electron Microscopy, Phys. Rev. Lett. **74**, 399 (1995).

[22] A. Tonomura, in *Electron Holography* (Springer, New York, 1999), pp. 29–49, https://link.springer.com/book/10.1007%2F978-3-540-37204-2.

[23] K. Harada, A. Tonomura, Y. Togawa, T. Akashi, and T. Matsuda, Double-biprism electron interferometry, Appl. Phys. Lett. **84**, 3229 (2004).

[24] F. Hasselbach, Progress in electron- and ion-interferometry, Rep. Prog. Phys. **73**, 016101 (2010).

[25] L. Marton, J. A. Simpson, and J. A. Suddeth, An electron interferometer, Rev. Sci. Instrum. **25**, 1099 (1954).

[26] B. M. Mertens, *Electron Microscopy with Standing Wave Illumination* (Delft University Press, Delft, 1999), oCLC: 839580419, https://repository.tudelft.nl/islandora/object/uuid:0bfd45ee-d517-4437-8b53-d12e91e4d42b?collection=research.

[27] B. Mertens and P. Kruit, Results of a pilot experiment on direct phase determination of diffracted beams in TEM, in *Electron Microscopy and Analysis Group Conf. EMAG99, Sheffield*, Institute of Physics Conference Series No. 161 (Institute of Physics, Bristol, 1999), pp. 133–136.

[28] A. Agarwal, C.-S. Kim, R. Hobbs, D. v. Dyck, and K. K. Berggren, A nanofabricated, monolithic, path-separated electron interferometer, Sci. Rep. **7,** 1677 (2017).

[29] A. H. Tavabi, M. Duchamp, V. Grillo, R. E. Dunin-Borkowski, and G. Pozzi, New experiments with a double crystal electron interferometer, Eur. Phys. J. Appl. Phys. **78,** 10701 (2017).

[30] G. Gronniger, B. Barwick, and H. Batelaan, A three-grating electron interferometer, New J. Phys. **8,** 224 (2006).

[31] F. S. Yasin, T. R. Harvey, J. J. Chess, J. S. Pierce, and B. J. McMorran, Path-separated electron interferometry in a scanning transmission electron microscope, J. Phys. D: Appl. Phys. **51,** 205104 (2018).

[32] F. S. Yasin, T. R. Harvey, J. J. Chess, J. S. Pierce, C. Ophus, P. Ercius, and B. J. McMorran, Probing light atoms at subnanometer resolution: realization of scanning transmission electron microscope holography, Nano Lett. **18,** 7118 (2018).

[33] T. R Harvey, J. S Pierce, A. K Agrawal, P. Ercius, M. Linck, and B. J. McMorran, Efficient diffractive phase optics for electrons, New J. Phys. **16,** 093039 (2014).

[34] C. W. Johnson, D. H. Bauer, and B. J. McMorran, Improved control of electron computer-generated holographic grating groove profiles using ion beam gas-assisted etching, Appl. Opt. **59,** 1594 (2020).

[35] B. J. McMorran, A. Agrawal, P. A. Ercius, V. Grillo, A. A. Herzing, T. R. Harvey, M. Linck, and J. S. Pierce, Origins and demonstrations of electrons with orbital angular momentum, Phil. Trans. R. Soc. A **375,** 20150434 (2017).

[36] D. L. Freimund, K. Aflatooni, and H. Batelaan, Observation of the Kapitza–Dirac effect, Nature (London) **413,** 142 (2001).

[37] N. Abedzadeh, M. A. R. Krielaart, C.-S. Kim, J. Simonaitis, R. Hobbs, P. Kruit, and K. K. Berggren, Electrostatic electron mirror in SEM for simultaneous imaging of top and bottom surfaces of a sample, arXiv:2012.09902.

[38] N. Abedzadeh, Diffractive electron mirror for use in quantum electron microscopy, Master's thesis, Massachusetts Institute of Technology, Department of Electrical Engineering and Computer Science, 2018, http://hdl.handle.net/1721.1/115627.

[39] P. Mooney, Optimization of image collection for cellular electron microscopy, in *Methods in Cell Biology*, Cellular Electron Microscopy Vol. 79 (Academic Press, New York, 2007), pp. 661–719, https://doi.org/10.1016/S0091-679X(06)79027-6.

[40] G. McMullan, S. Chen, R. Henderson, and A. R. Faruqi, Detective quantum efficiency of electron area detectors in electron microscopy, Ultramicroscopy **109,** 1126 (2009).

[41] Y. Jia, B. Mollon, P. Mooney, M. Pan, B. McGinn, M. Azimi, N. Cabilan, A. Gubbens, and M. Lent, A new high speed, high resolution 2k x 2k CCD Camera for Transmission Electron Microscopes, Microsc. Microanal. **17,** 814 (2011).

[42] S. L. Y. Chang, C. Dwyer, J. Barthel, C. B. Boothroyd, and R. E. Dunin-Borkowski, Performance of a direct detection camera for off-axis electron holography, Ultramicroscopy **161,** 90 (2016).

[43] G. McMullan, A. R. Faruqi, D. Clare, and R. Henderson, Comparison of optimal performance at 300 keV of three direct electron detectors for use in low dose electron microscopy, Ultramicroscopy **147,** 156 (2014).

[44] X. Sang and J. M. LeBeau, Characterizing the response of a scintillator-based detector to single electrons, Ultramicroscopy **161,** 3 (2016).

[45] J. A. Mir, R. Clough, R. MacInnes, C. Gough, R. Plackett, I. Shipsey, H. Sawada, I. MacLaren, R. Ballabriga, D. Maneuski, V. O'Shea, D. McGrouther, and A. I. Kirkland, Characterisation of the Medipix3 detector for 60 and 80 keV electrons, Ultramicroscopy **182,** 44 (2017).

[46] L. Vaidman, The meaning of the interaction-free measurements, Found. Phys. **33,** 491 (2003).

[47] A. Greenberg, B. McMorran, C. Johnson, and F. Yasin, Magnetic phase imaging using interferometric STEM, Microsc. Microanal. **26,** 2480 (2020).

[48] Y. Takahashi, Y. Yajima, M. Ichikawa, and K. Kuroda, Observation of magnetic induction distribution by scanning interference electron microscopy, Jpn. J. Appl. Phys. **33,** L1352 (1994).

[49] A. Tonomura, N. Osakabe, T. Matsuda, T. Kawasaki, J. Endo, S. Yano, and H. Yamada, Evidence for Aharonov-Bohm Effect with Magnetic Field Completely Shielded from Electron Wave, Phys. Rev. Lett. **56,** 792 (1986).

[50] A. Caprez, B. Barwick, and H. Batelaan, Macroscopic Test of the Aharonov-Bohm Effect, Phys. Rev. Lett. **99,** 210401 (2007).

[51] C. Ophus, J. Ciston, J. Pierce, T. R. Harvey, J. Chess, B. J. McMorran, C. Czarnik, H. H. Rose, and P. Ercius, Efficient linear phase contrast in scanning transmission electron microscopy with matched illumination and detector interferometry, Nat. Commun. **7,** 10719 (2016).

[52] R. Egerton, Radiation damage to organic and inorganic specimens in the TEM, Micron **119,** 72 (2019).

[53] R. W. M. Hooley, A. P. Brown, A. N. Kulak, F. C. Meldrum, and R. M. D. Brydson, A quantitative evaluation of electron beam sensitivity in calcite nanoparticles, J. Phys. Conf. Ser. **902,** 012005 (2017).

[54] M. Pan and P. Crozier, Quantitative imaging and diffraction of zeolites using a slow-scan CCD camera, Ultramicroscopy **52,** 487 (1993).

[55] P. Li and R. Egerton, Radiation damage in coronene, rubrene and p-terphenyl, measured for incident electrons of kinetic energy between 100 and 200 kev, Ultramicroscopy **101,** 161 (2004).

[56] R. Egerton, P. Crozier, and P. Rice, Electron energy-loss spectroscopy and chemical change, Ultramicroscopy **23,** 305 (1987).